Advanced Steel Construction – Vol. 20 No. 1 (2024) 81–92
DOI:10.18057/IJASC.2024.20.1.9

STRUCTURAL MORPHOLOGY AND DYNAMIC CHARACTERISTICS ANALYSIS OF DRUM-SHAPED HONEYCOMB-TYPE III CABLE DOME WITH QUAD-STRUT LAYOUT

Hui Lv [1, 2, *], Hao Zhang [1], Zhong-Yi Zhu [3], Shi-Lin Dong [2] and Xin Xie [1]

[1] *College of Civil Engineering and Architecture, Nanchang Hangkong University, Nanchang 330063, China*
[2] *Space Structures Research Center, Zhejiang University, Hangzhou 310058, China*
[3] *Beijing Institute of Architectural Design,Beijing 100045,China;*
** (Corresponding author: E-mail: lvhui@nchu.edu.cn)*

ABSTRACT

The drum-shaped honeycomb-type III cable dome with a quad-strut layout abandons the traditional concept, incorporating a multi-support pole concept, making it one of the most structurally diverse types of cable dome structures. Its upper chord cable mesh is evenly divided, resulting in a simple and efficient structural design. This design approach reduces the usage of cables and struts, making pre-stressing and tensioning construction more convenient. Furthermore, the structure exhibits good cost-effectiveness. Based on the node force equilibrium equations, a general formula is derived for calculating the internal forces of prestressed cables and struts in the prestressed state of the structure. Additionally, the variation of prestress distribution with geometric parameters of the cable dome structure is analyzed. A numerical model with a span of 120 meters was established in the general finite element software Ansys to investigate the influence of structural parameters on the structural natural frequency characteristics. Moreover, using the nonlinear dynamic analysis method, the dynamic response of the structure under multidimensional seismic loads was compared and analyzed. The research results indicate that the prestress distribution of the structure is reasonable, with a greater amount of prestress in the outer ring compared to the inner ring. This observation suggests that the stiffness of the structure is primarily supported by the outer ring structure. The structural natural modes of vibration predominantly exhibit vertical deformation, indicating that the vertical stiffness of the structure is weaker than the circumferential direction. Furthermore, when subjected to seismic loading, the internal forces in cables and struts, as well as the dynamic displacements of key nodes, are relatively small, demonstrating excellent seismic performance.

ARTICLE HISTORY

Received: 4 November 2023
Revised: 5 February 2024
Accepted: 7 February 2024

KEYWORDS

Drum-shaped honeycomb-type;
Structural morphology analysis;
Parametric analysis;
Natural vibration mode;
Seismic analysis

1. Introduction

The concept of prestressing the entire structure was initially proposed by the American engineer Fuller, who envisioned a structural system that remains continuously under tension as a whole while experiencing discrete areas of compression. The fundamental idea behind this concept is that "compressed islands exist in the ocean of tension" [1]. In the 1980s, the American engineer Geiger further evolved and developed Fuller's ideas, introducing the Geiger-type cable dome structure, which was successfully applied in the construction of the sports arena and fencing hall for the 1988 Seoul Olympics [2,3]. To address the issues of weak out-of-plane stiffness and limited capacity to withstand asymmetric loads in the Geiger-type cable dome structure, the American engineer Levy proposed the Levy-type cable dome structure. This design incorporates triangular spatial trusses internally, significantly enhancing the overall stability of the structure. The Levy-type cable dome structure found successful application in the main stadium, Georgia Dome, during the 1996 Atlanta Olympics [4]. However, this structural arrangement increases the number of struts, due to the dense grid division in the inner ring, making the construction of inner ring nodes and membrane installation more challenging [5].

In order to address the issues encountered in the two classic cable dome structural forms, in 2005, Shilin Dong et al. proposed the Kewitte-type cable dome and two hybrid cable domes, incorporating the arrangement patterns of various grid shell structures into the cable dome structures [6]. All of these structures feature advantages such as uniform grid division and even stiffness distribution. In 2010, Shilin Dong et al. introduced an innovative spatial structural system that combines a single-layer grid shell with a cable dome [7]. Subsequently, Shilin Dong et al. introduced a new type of honeycomb-type cable dome with a multi-strut layout structural system [8,9]. In this cable dome design, the upper chord consists of ridge cables arranged in a honeycomb pattern, while multiple support struts connect to the lower chord nodes. After the introduction of the innovative research on the honeycomb-type cable dome structural system, Shilin Dong and Hui Lv et al. have recently proposed the drum-shaped honeycomb-type cable dome with a quad-strut layout [10]. This concept deviates from the traditional cable dome concept that typically involves tension cables and compressed strut islands. Instead, it incorporates the idea of multiple support struts, resulting in three cable dome structural forms: the drum-shaped honeycomb-type I, II, and III cable domes with a quad-strut layout. The analysis methods for determining the prestressed state of these three cable dome structures have also been explored.

The cable dome structure is a typical flexible structure where its structural stiffness is primarily provided by prestressing. Therefore, the analysis of prestressed modes and structural morphology is the foundation and key to the theoretical analysis of cable dome structures. Pellegrino et al. proposed the theory of equilibrium matrices [11,12]. For structures with known geometric dimensions and topological relationships, the relationship between the structural member topology and internal forces can be expressed in matrix form using node equilibrium equations. Furthermore, Xingfei Yuan et al. introduced the concept of globally feasible prestress modes for cable domes, taking advantage of the structure's symmetry. They employed the method of quadratic singular value decomposition to determine prestress modes that would ensure geometric stability in cable dome structures [13].

Regarding cable dome structures, which are characterized by flexibility, lightness, large spans and significant nonlinearity, researchers in the field have conducted extensive studies on their dynamic characteristics. Pengcheng Li et al. explored the natural vibration characteristics of the cable-stiffened single-layer latticed shell through modal analysis. They also analyzed the structure's nonlinear behavior when subjected to the El Centro earthquake waves [14]. In a separate study, Zhenwei Li et al. investigated the internal connections between multiple square loop-string cables and grid beams, providing valuable insights for seismic-resistant structures [15]. Hao Zhang et al. analyzed the dynamic response of the cable dome structure, specifically focusing on the consequences of local cable or strut failures, distinguishing the importance of structural cables and struts [16]. Chi Zhu et al. have introduced a method aimed at enhancing the efficiency of structural dynamic testing and propose a dynamic response reconstruction method that accounts for step excitation, alongside a corresponding high-precision non-measurement point selection strategy [17]. However, regarding the drum-shaped honeycomb-type cable dome, current research has only focused on the static performance of the structure.

Accordingly, this paper aims to further investigate the mechanical characteristics of the novel drum-shaped honeycomb-type III cable dome with a quad-strut layout. Based on the node equilibrium equations and under the conditions of symmetry and periodicity, analytical formulas for the prestressed cable forces in the structure were derived. Additionally, the paper analyzed the influence of various design parameters on the distribution of prestressing forces within the structure. By considering a 120 m cable dome as an example, the paper analyzed the natural frequency characteristics of the structure and

investigated the impact of various structural parameters on these characteristics. Building upon the results of the natural frequency analysis, a time history analysis method was employed to calculate the dynamic responses of cable forces in different struts and the displacements of key nodes under multidimensional seismic loads. This analysis provided valuable insights into the structure's ability to withstand seismic forces. The research finding provides a reference for the practical engineering design of this specific cable dome configuration.

2. Structural configuration and pre-stress state analysis

2.1. Structural configuration

As shown in Fig. 1, the main structure of the drum-shaped honeycomb-type III cable dome with a quad-strut layout is composed of ridge cables, ring cables, diagonal cables, struts and rigid ring beams. In Figs. 1a and 1b, the labels *N*, *T*, *B*, *H*, and *V* represent the upper chord circumferential ridge cables, radial ridge cables, diagonal cables, ring cables and struts respectively. The subscripted numbers indicate the concentric circles from the inside out, while the letters indicate the types of components. Within the main hexagonal grid of the upper chord, two diagonal cables and four struts are arranged in a skip pattern. The lower chord nodes are positioned along the radial axis of the main hexagonal grid, and ring cables connect each lower chord node. Additionally, the inner upper chord ridge cable connects two adjacent main hexagonal grids, forming secondary hexagonal grids.

For the drum-shaped honeycomb-type cable dome with a multi-strut layout, it can be represented usingthe symbol ${}_n\overline{H}_{ms}$ with three subscripts, where *n* represents the number of circumferential divisions, *m* represents the number of ring cables, and *s* represents the number of struts converging at the lower chord nodes. The structure shown in Fig. 1 can be denoted by the symbol ${}_{24}\overline{H}_{24\mathrm{III}}$, where III indicates the upper chord ridge cable arrangement scheme.

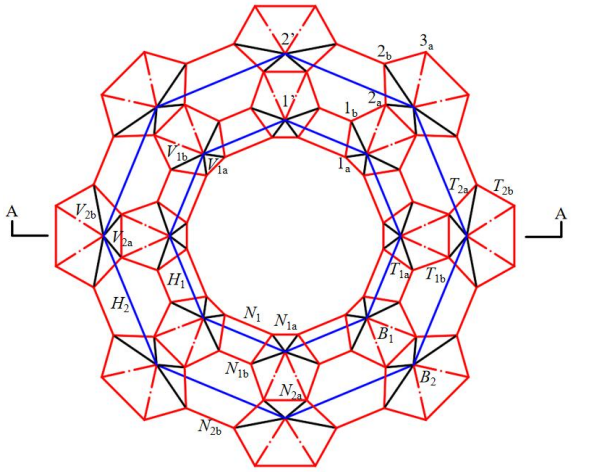

(a) Schematic plan

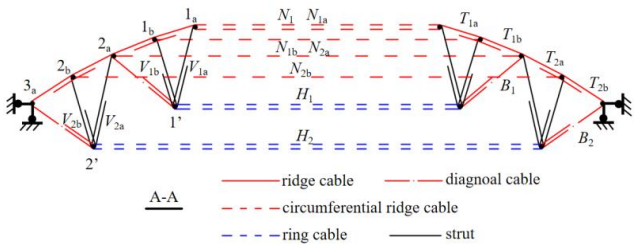

(b) Sectional view (A-A)

Fig. 1 Schematic diagram of the ${}_{24}\overline{H}_{24\mathrm{III}}$ cable dome

The advantages of the ${}_{24}\overline{H}_{24\mathrm{III}}$ cable dome are as follows:

(1) The upper chord ridge cable grid of the ${}_{24}\overline{H}_{24\mathrm{III}}$ cable dome is evenly divided, inheriting the advantages of simplicity and efficiency from the drum-shaped honeycomb-type cable dome with a multi-strut layout. This design feature allows the cable dome to adapt to a variety of circumferential broken-line cable dome shapes, meeting the architectural design requirements.

(2) There are a total of 8 pairs of outer ring diagonal cables in the structure. Simultaneously tensioning all outer ring diagonal cables can effectively reduce the risk of ring cable slippage.

(3) There are 4 compression struts converging at the lower chord node of the ${}_{24}\overline{H}_{24\mathrm{III}}$ cable dome, forming a continuous double-V spatial structure in the circumferential direction. This spatial configuration enhances the lateral stiffness at the upper and lower nodes. Additionally, the number of components converging at the inner and outer upper chord nodes is 4 and 5 respectively, creating a spatial load-bearing system. This design significantly improves the stability and load-bearing performance of the entire cable dome structure, making it suitable for the use of a rigid roof system.

(4) The strut-to-cable quantity ratio of the ${}_{24}\overline{H}_{24\mathrm{III}}$ cable dome is only 1:1.9, which is significantly lower compared to ratios of 1:3 for Gerger-type cable domes and 1:5 for Levy-type cable domes [18]. This suggests that the ${}_{24}\overline{H}_{24\mathrm{III}}$ cable dome is more economical, considering that the cost of cable materials is typically higher than that of rod materials.

2.2. Analysis method of prestressed state

The ${}_{24}\overline{H}_{24\mathrm{III}}$ cable dome structure simplifies the analysis and computation process by considering a single substructure when the spatial arrangement meets axial symmetry conditions and is divided into n equal parts in the circumferential direction. The analysis and computation of the substructure should refer to the plan and section diagrams shown in Fig. 2. The internal forces of each component should be labeled with the respective component names. The angles between the upper chord cables, struts, diagonal cables and the horizontal plane are denoted as α_{ia}, α_{ib}, ϕ_{ia}, ϕ_{ib}, β_i respectively. Under the action of axially symmetric prestress, by establishing the equilibrium equations for the nodal forces, it is possible to calculate the relationships between the internal forces of cables and struts in the cable dome structure. For nodes located on two symmetric axes simultaneously, a vertical force equilibrium equation can be established. For nodes along the radial symmetric axis, two equilibrium equations can be established. For general nodes that do not align with a symmetric axis, three node equilibrium equations can be established.

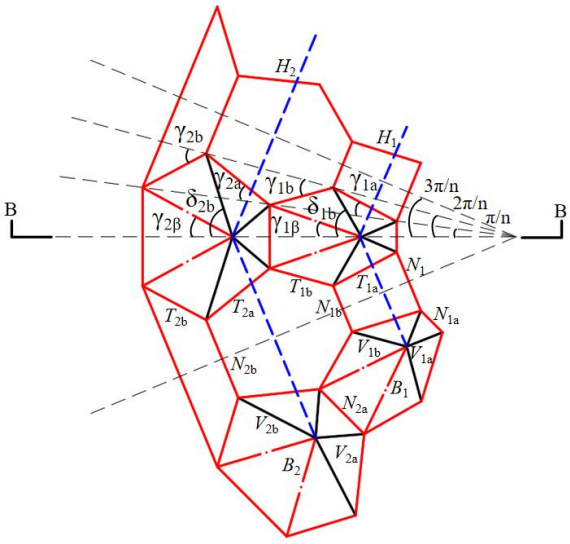

(a) Analysis model (plan view)

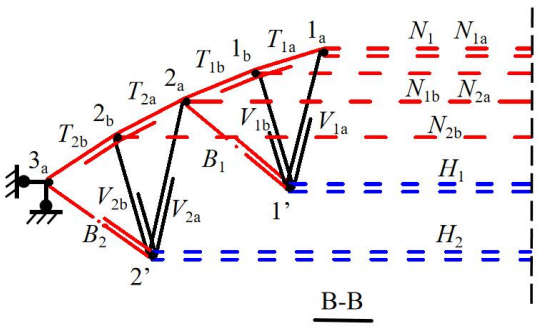

(b) Sectional view (B-B)

Fig. 2 Analysis model of the ${}_{24}\overline{H}_{24\mathrm{III}}$ cable dome

For the ${}_{24}\bar{H}_{24\mathrm{III}}$ cable dome, there are a total of 17 types of components. Equations (1) - (6) collectively form a set of 16 node equilibrium equations. The number of these equations is one less than the number of unknown internal forces in the cables and struts. Therefore, this structure is classified as a statically determinate structure of the first degree. The nodal equilibrium equation group is as follows:

For node 1_a:

$$\left.\begin{aligned}
&\bullet\ T_{1a}\cos\alpha_{1a}\cos\gamma_{1a}+V_{1a}\cos\varphi_{1a}\cos(\delta_{1\mathbf{a}}+\frac{\pi}{\mathrm{n}})\ =N_1\sin\frac{2\pi}{\mathrm{n}}+N_{1a}\sin\frac{\pi}{\mathrm{n}}\\
&\bullet\ T_{1a}\cos\alpha_{1a}\sin\gamma_{1a}-V_{1a}\cos\varphi_{1a}\sin(\delta_{1\mathbf{a}}+\frac{\pi}{\mathrm{n}})=N_{1a}\cos\frac{2\pi}{\mathrm{n}}-N_1\cos\frac{\pi}{\mathrm{n}}\\
&\bullet\ T_{1\mathbf{a}}\sin\beta_{1a}+2V_{1a}\sin\varphi_{1a}=0
\end{aligned}\right\}\quad(1)$$

For node 1':

$$\left.\begin{aligned}
&\bullet\ 2B_1\cos\beta_1\cos\gamma_{1\beta}+2V_{1b}\cos\phi_{1b}\cos\delta_{1b}\ =2H_1\sin\frac{3\pi}{n}\\
&\quad+2V_{1a}\cos\phi_{1a}\cos\delta_{1a}\\
&\bullet\ 2B_1\cos\beta_1+2V_{1b}\sin\phi_{1b}+2V_{1a}\sin\phi_{1a}=0
\end{aligned}\right\}\quad(2)$$

For node 1_b:

$$\left.\begin{aligned}
&\bullet\ T_{1b}\cos\alpha_{1\mathbf{b}}\cos\gamma_{1b}=T_{1a}\cos\alpha_{1a}\cos(\gamma_{1\mathbf{a}}-\frac{\pi}{n})\\
&\quad+V_{1b}\cos\phi_{1b}\cos(\delta_{1b}-\frac{2\pi}{n})\ N_{1b}\sin\frac{\pi}{n}\\
&\bullet\ T_{1b}\cos\alpha_{1\mathbf{b}}\sin\gamma_{1b}+T_{1a}\cos\alpha_{1a}\sin(\gamma_{1\mathbf{a}}-\frac{\pi}{n})\\
&\quad+V_{1b}\cos\phi_{1b}\sin(\delta_{1b}-\frac{2\pi}{n})\ -N_{1b}\cos\frac{\pi}{n}\\
&\bullet\ T_{1b}\sin\alpha_{1\mathbf{b}}-T_{1a}\sin\alpha_{1\mathbf{a}}+V_{1b}\sin\phi_{1b}=0
\end{aligned}\right\}\quad(3)$$

For node 2_a:

$$\left.\begin{aligned}
&\bullet\ T_{2a}\cos\alpha_{1a}\cos\gamma_{2\mathbf{a}}+V_{2a}\cos\phi_{2a}\cos(\delta_{2a}+\frac{\pi}{n})\\
&\quad=T_{1b}\cos\alpha_{1b}\cos(\gamma_{1b}-\frac{\pi}{n})\ +B_1\cos\beta_1\cos(\gamma_{1\beta}-\frac{\pi}{n})\\
&\quad+N_{2a}\sin\frac{\pi}{n}\\
&\bullet\ T_{2a}\cos\alpha_{2a}\sin\gamma_{2a}-V_{2a}\cos\phi_{2a}\sin(\delta_{2a}+\frac{\pi}{n})\\
&\quad+T_{1b}\cos\alpha_{1b}\sin(\gamma_{1b}-\frac{\pi}{n})-B_1\cos\beta_1\sin(\gamma_{1\beta}-\frac{\pi}{n})\\
&\quad-N_{2a}\cos\frac{\pi}{n}=0\\
&\bullet\ T_{2a}\sin\alpha_{2a}+V_{2a}\sin\phi_{2a}-T_{1b}\sin\alpha_{1b}\\
&\quad+B_1\cos\beta_1=0
\end{aligned}\right\}\quad(4)$$

For node 2':

$$\left.\begin{aligned}
&\bullet\ 2B_2\cos\beta_2\cos\gamma_{2\beta}+2V_{2b}\cos\phi_{2b}\cos\delta_{2b}\\
&\quad=2H_2\sin\frac{3\pi}{n}\ +2V_{2a}\cos\phi_{2a}\cos\delta_{2a}\\
&\bullet\ 2B_2\sin\beta_2+2V_{2b}\sin\phi_{2b}+2V_{2a}\sin\phi_{2a}\\
&\quad=0
\end{aligned}\right\}\quad(5)$$

For node 2_b:

$$\left.\begin{aligned}
&\bullet\ T_{2b}\cos\alpha_{2b}\cos\gamma_{\mathbf{2b}}=T_{2a}\cos\alpha_{2a}\cos(\gamma_{2\mathbf{a}}-\frac{2\pi}{n})\\
&\quad+V_{2b}\cos\phi_{2b}\cos(\delta_{2a}-\frac{\pi}{n})+N_{2b}\sin\frac{\pi}{n}\\
&\bullet\ T_{2b}\cos\alpha_{2b}\sin\gamma_{2b}+T_{2a}\cos\alpha_{2a}\sin(\gamma_{2\mathbf{a}}-\frac{2\pi}{n})\\
&\quad+V_{2b}\cos\phi_{2b}\sin(\delta_{2a}-\frac{\pi}{n})-N_{2b}\cos\frac{\pi}{n}=0\\
&\bullet\ T_{2b}\sin\alpha_{2b}+V_{2b}\sin\phi_{2b}-T_{2b}\sin\alpha_{2a}=0
\end{aligned}\right\}\quad(6)$$

The support reactions under prestressed conditions can also be determined using the following equations:

$$\left.\begin{aligned}
&\bullet\ X=\begin{bmatrix}B_2\cos\beta_2\cos\left(\gamma_{2\beta}-\frac{\pi}{n}\right)\\+T_{2b}\cos\alpha_{2b}\cos\left(\gamma_{2b}-\frac{\pi}{n}\right)\end{bmatrix}\\
&\bullet\ Y=\pm\begin{bmatrix}B_2\cos\beta_2\sin\left(\gamma_{2\beta}-\frac{\pi}{n}\right)\\-T_{2b}\cos\alpha_{2b}\sin\left(\gamma_{2b}-\frac{\pi}{n}\right)\end{bmatrix}
\end{aligned}\right\}\quad(7)$$

In conclusion, based on the node force equilibrium equations for a single substructure, formulas for calculating the internal forces in various types of cables and struts have been derived. These formulas are specifically applicable for determining the internal force distribution in the prestressed state of the ${}_{24}\bar{H}_{24\mathrm{III}}$ cable dome with a planar projection in the shape of a circle, while satisfying periodicity and symmetry conditions.

3. Parametric analysis of prestressed state

3.1. Structural design parameters

For the ${}_{24}\bar{H}_{24\mathrm{III}}$ cable dome with a span of L, inner ring opening size of L_0, spherical shell radius of R, rise height of f and structural thickness of h, the simplified half-space truss, considering periodicity and symmetry conditions, is shown in Fig. 3. The calculation formulas for the main geometric parameters are listed in Table 1.

The thickness h_i and length Δ_{ia}, Δ_{ib} of the cable dome are determined separately using the following equations (8) and (9). The thickness h represents the center thickness of the cable dome, while h_i varies linearly along the radial direction. ζ and η_i are dimensionless coefficients.

$$h_i=h\left(1\pm\xi\frac{r_i}{r}\right)\qquad i=(1,2)\quad(8)$$

$$\frac{\Delta_{ia}}{\Delta_{ib}}=\eta_i\quad(9)$$

As illustrated in Fig. 3, the arrangement schemes for the lower chord node i' of the structure includes three cases:

Case 1: The projected length of the two inner struts in the horizontal plane radial direction is 0, as shown in Fig. 3a.

Case 2: The projected length of the two inner struts in the horizontal plane radial direction is $\Delta_{ia}/2$, as shown in Fig. 3b.

Case 3: The projected length of the two inner struts in the horizontal plane radial direction is Δ_{ia}, as shown in Fig. 3c.

Based on the above, the primary design parameters for the form of the cable dome structure include the span-to-rise ratio, thickness-to-span ratio and the arrangement scheme for the lower chord nodes i'. Once these design parameters are established, the geometric configuration of the structure can be determined using the formulas provided in Table 1. Furthermore, the prestress distribution within the cable dome can be determined using equations (1) to (7).

Table 1
Formula for calculating the geometric dimensions of the $_{24}H_{24III}$ type cable dome (i=1, 2)

Length parameter	Angle parameters
$R = L^2/8_f + \frac{f}{2}$ $\quad r = R\sin\theta$	
$r_{ia} = R\sin\theta_{ia} = r_{(i+1)a} - (\Delta_{ia} + \Delta_{ib})$	
$r_{ib} = R\sin\theta_{ib} = r_{(i+1)a} - \Delta_{ib}$ $\quad r' = r_i = R\sin\theta_i$	
$s_{ia} = \sqrt{(r_{ib}\cos\frac{\pi}{n} - r_{ia})^2 + (r_{ib}\sin\frac{\pi}{n})^2}$	$\alpha_{ia} = \tan^{-1}(\frac{h_{ia}}{s_{ia}})$ $\quad \alpha_{ib} = \tan^{-1}(\frac{h_{ib}}{s_{ib}})$
$s_{ib} = \sqrt{(r_{(i+1)a}\cos\frac{\pi}{n} - r_{ib})^2 + (r_{(i+1)a}\sin\frac{\pi}{n})^2}$	$\varphi_{ia} = \tan^{-1}(\frac{h'_{ia}}{s'_{ia}})$ $\quad \varphi_{ib} = \tan^{-1}(\frac{h'_{ib}}{s'_{ib}})$
$s'_{ia} = \sqrt{(r_i - r_{ia}\cos\frac{\pi}{n})^2 + (r_{ia}\sin\frac{\pi}{n})^2}$	$\beta_i = \tan^{-1}(\frac{h'_i}{s'_i})$ $\quad \gamma_{ia} = \tan^{-1}(\frac{r_{ib}\sin\frac{\pi}{n}}{r_{ib}\cos\frac{\pi}{n} - r_{ia}})$
$s'_{ib} = \sqrt{(r_b\cos\frac{\pi}{n} - r_i)^2 + (r_{ib}\sin\frac{\pi}{n})^2}$	$\gamma_{ib} = \tan^{-1}(\frac{r_{(i+1)a}\sin\frac{\pi}{n}}{r_{(i+1)a}\cos\frac{\pi}{n} - r_{ib}})$ $\quad \delta_{ia} = \tan^{-1}(\frac{r_{ia}\sin\frac{\pi}{n}}{r_i - r_{ia}\cos\frac{\pi}{n}})$
$s'_i = \sqrt{(r_{(i+1)a}\cos\frac{\pi}{n} - r_i)^2 + (r_{(i+1)a}\sin\frac{\pi}{n})^2}$	$\delta_{ib} = \tan^{-1}(\frac{r_{ib}\sin\frac{2\pi}{n}}{r_{ib}\cos\frac{2\pi}{n} - r_i})$ $\quad \gamma_{i\beta} = \tan^{-1}(\frac{r_{(i+1)a}\sin\frac{\pi}{n}}{r_{(i+1)a}\cos\frac{\pi}{n} - r_i})$
$h_{ia} = R(\cos\theta_{ia} - \cos\theta_{ib})$ $\quad h_{ib} = R(\cos\theta_{ib} - \cos\theta_{(i+1)a})$	
$h'_{ia} = h_i + R(\cos\theta_{ia} - \cos\theta_i)$ $\quad h'_{ib} = h_i + R(\cos\theta_{ib} - \cos\theta_i)$	
$h'_i = h_i - R(\cos\theta_i - \cos\theta_{(i+1)a})$	

Note: h_{ia}, h_{ib}, h'_{ia}, h'_{ib}, h'_i represent the height of the upper chord cables, struts and diagonal cables respectively, S_{ia}, S_{ib}, S'_{ia}, S'_{ib}, S'_i represent the horizontal projected lengths of the upper chord cables, struts and diagonal cables respectively.

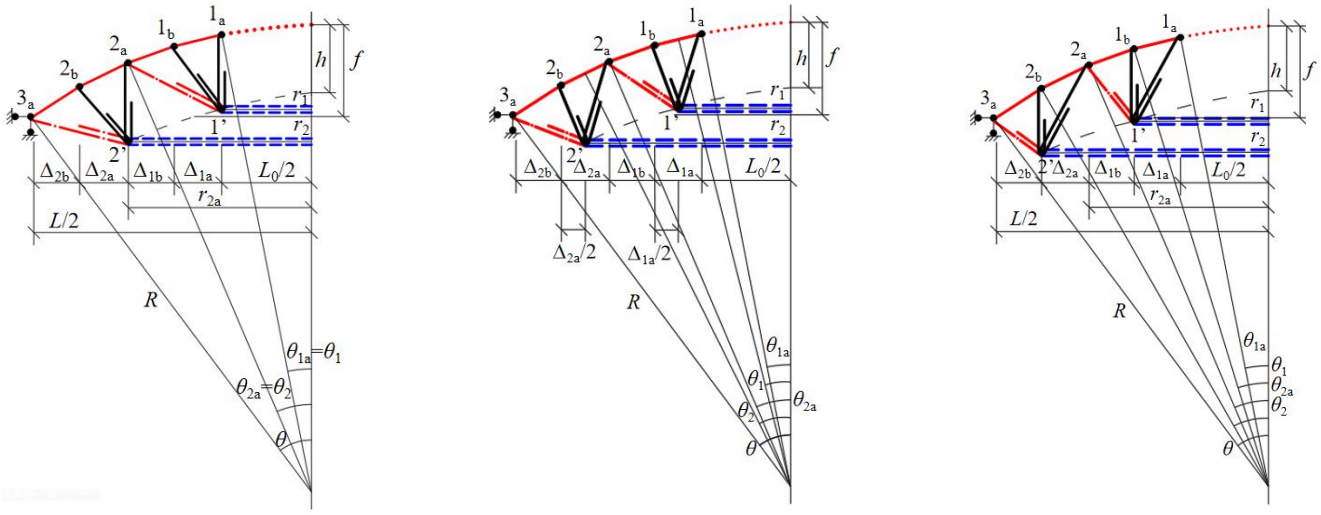

(a) Case 1 (b) Case2 (c) Case 3

Fig. 3 The arrangement schemes for the lower chord node *i*'

3.2. Parametric analysis example of prestress distribution

In the parametric analysis, the span-to-rise ratio was set to 0.08, 0.09 and 0.10, while the thickness-to-span ratio was set to 0.07, 0.08, 0.09 and 0.10. The parameter η was set to 1.0. The cable dome structure had a span (L) of 120 m, an inner ring opening diameter (L_0) of 40 m, and both Δ_{ia} and Δ_{ib} equal to 10 m. Under the relative prestress H_2 = 1.0, the prestressed cable dome structure's internal force distribution in cables and struts can be determined. Prestressed state analysis was implemented using a custom code developed on the Matlab platform, and the calculated results are shown in Table 2. Through comparison with the case study, the calculated results were found to be consistent with the results obtained from the second-order singular value decomposition method [19].

By observing the calculated results in Table 2, the following patterns can be summarized:

(1) When the span-to-rise ratio (f/L) and the thickness-to-span ratio (h/L) are equal for the cable dome, and the same lower chord node arrangement scheme is used, the internal forces in cables and struts exhibit geometrically equal patterns under prestressed conditions.

(2) Under prestressed state, the internal forces in cables and struts, including support reactions, increase linearly with an increasing thickness-to-span ratio. This indicates that as the structural stiffness increases, the internal forces in cables and struts also increase accordingly.

(3) Under prestressed state, the internal force distribution in the cables and struts of the outer ring of the cable dome structure is significantly greater than that of the inner ring, indicating that the structural stiffness is mainly contributed by the outer ring structure.

(4) Among the three lower chord node arrangement schemes, Case 1 is less affected by changes in the span-to-rise ratio and thickness-to-span ratio in terms of internal forces in cables and struts. Case 2 is relatively more sensitive, while Case 3 is the most sensitive to these changes.

Table 2
The distribution of prestress in the cable dome structure under changes in geometric parameters

Parameter	f/L	0.08				0.09				0.10			
	h/L	0.07	0.08	0.09	0.10	0.07	0.08	0.09	0.10	0.07	0.08	0.09	0.10
Case 1	H_2	1.00	1.00	1.00	1.00	1.00	1.00	1.00	1.00	1.00	1.00	1.00	1.00
	N_1	0.21	0.30	0.41	0.52	0.13	0.21	0.30	0.39	0.08	0.15	0.22	0.30
	N_{1a}	0.24	0.35	0.47	0.60	0.15	0.25	0.35	0.45	0.09	0.17	0.26	0.35
	N_{1b}	0.07	0.10	0.14	0.18	0.04	0.07	0.10	0.13	0.02	0.05	0.07	0.10
	T_{1a}	0.09	0.14	0.18	0.23	0.06	0.10	0.13	0.18	0.03	0.07	0.10	0.13
	T_{1b}	0.10	0.15	0.21	0.27	0.06	0.11	0.15	0.20	0.04	0.07	0.11	0.15
	V_{1a}	-0.01	-0.02	-0.02	-0.03	-0.01	-0.01	-0.02	-0.02	-0.01	-0.01	-0.02	-0.02
	V_{1b}	-0.01	-0.01	-0.02	-0.02	-0.01	-0.01	-0.02	-0.02	0.00	-0.01	-0.01	-0.02
	B_1	0.07	0.08	0.10	0.11	0.05	0.07	0.08	0.10	0.04	0.06	0.07	0.08
	H_1	0.15	0.18	0.20	0.22	0.11	0.15	0.18	0.20	0.08	0.12	0.15	0.17
	N_{2a}	0.20	0.28	0.36	0.40	0.14	0.21	0.28	0.35	0.09	0.15	0.21	0.28
	N_{2b}	0.24	0.34	0.44	0.54	0.16	0.25	0.33	0.43	0.10	0.17	0.25	0.33
	T_{2a}	0.23	0.31	0.40	0.49	0.16	0.24	0.31	0.39	0.10	0.17	0.24	0.31
	T_{2b}	0.26	0.37	0.49	0.60	0.18	0.28	0.37	0.47	0.11	0.20	0.28	0.37
	V_{2a}	-0.05	-0.07	-0.09	-0.11	-0.04	-0.06	-0.08	-0.10	-0.03	-0.05	-0.07	-0.09
	V_{2b}	-0.04	-0.06	-0.07	-0.08	-0.03	-0.05	-0.06	-0.07	-0.02	-0.04	-0.05	-0.06
	B_2	0.44	0.45	0.46	0.47	0.43	0.44	0.45	0.46	0.43	0.43	0.44	0.45
	X	0.64	0.73	0.83	0.93	0.56	0.65	0.73	0.82	0.50	0.58	0.65	0.73
	Y	-0.03	-0.08	-0.14	-0.20	0.02	-0.03	-0.08	-0.13	0.05	0.01	-0.04	-0.08
Case 2	H_2	1.00	1.00	1.00	1.00	1.00	1.00	1.00	1.00	1.00	1.00	1.00	1.00
	N_1	0.27	0.36	0.46	0.56	0.19	0.28	0.36	0.45	0.14	0.21	0.28	0.36
	N_{1a}	0.31	0.43	0.54	0.66	0.23	0.32	0.42	0.52	0.16	0.25	0.33	0.42
	N_{1b}	0.10	0.13	0.17	0.20	0.07	0.10	0.13	0.16	0.05	0.07	0.10	0.13
	T_{1a}	0.13	0.17	0.22	0.27	0.09	0.13	0.17	0.21	0.07	0.10	0.14	0.17
	T_{1b}	0.15	0.20	0.26	0.31	0.11	0.15	0.20	0.25	0.08	0.12	0.16	0.20
	V_{1a}	-0.02	-0.02	-0.03	-0.04	-0.02	-0.02	-0.03	-0.03	-0.01	-0.02	-0.02	-0.03
	V_{1b}	-0.01	-0.02	-0.02	-0.02	-0.01	-0.01	-0.02	-0.02	-0.01	-0.01	-0.02	-0.02
	B_1	0.07	0.08	0.09	0.10	0.06	0.07	0.08	0.09	0.05	0.06	0.07	0.08
	H_1	0.18	0.20	0.22	0.23	0.15	0.18	0.20	0.21	0.13	0.15	0.18	0.19
	N_{2a}	0.35	0.44	0.54	0.64	0.27	0.35	0.44	0.53	0.20	0.28	0.36	0.44
	N_{2b}	0.37	0.48	0.59	0.70	0.29	0.38	0.48	0.58	0.22	0.30	0.39	0.48
	T_{2a}	0.35	0.44	0.53	0.62	0.27	0.36	0.44	0.52	0.21	0.29	0.37	0.44
	T_{2b}	0.43	0.55	0.67	0.79	0.34	0.45	0.55	0.66	0.26	0.36	0.46	0.55
	V_{2a}	-0.09	-0.11	-0.13	-0.14	-0.08	-0.10	-0.12	-0.14	-0.07	-0.09	-0.11	-0.13
	V_{2b}	-0.07	-0.08	-0.09	-0.10	-0.06	-0.07	-0.08	-0.09	-0.05	-0.06	-0.07	-0.08
	B_2	0.42	0.42	0.43	0.44	0.42	0.42	0.43	0.44	0.42	0.42	0.43	0.44
	X	0.74	0.83	0.93	1.03	0.66	0.74	0.83	0.92	0.60	0.67	0.75	0.83
	Y	-0.08	-0.14	-0.20	-0.27	-0.03	-0.08	-0.14	-0.20	0.02	-0.04	-0.09	-0.14
Case 3	H_2	1.00	1.00	1.00	1.00	1.00	1.00	1.00	1.00	1.00	1.00	1.00	1.00
	N_1	0.33	0.42	0.52	0.62	0.26	0.34	0.42	0.51	0.20	0.27	0.35	0.42
	N_{1a}	0.39	0.50	0.62	0.73	0.31	0.40	0.50	0.60	0.24	0.33	0.41	0.50

Table 2
The distribution of prestress in the cable dome structure under changes in geometric parameters

Parameter	f/L	0.08				0.09				0.10			
	h/L	0.07	0.08	0.09	0.10	0.07	0.08	0.09	0.10	0.07	0.08	0.09	0.10
Case 3	N_{1b}	0.13	0.16	0.20	0.24	0.10	0.13	0.16	0.20	0.08	0.11	0.13	0.16
	T_{1a}	0.17	0.22	0.26	0.31	0.14	0.18	0.22	0.26	0.11	0.14	0.18	0.22
	T_{1b}	0.21	0.26	0.32	0.37	0.17	0.21	0.26	0.31	0.13	0.17	0.22	0.26
	V_{1a}	-0.03	-0.04	-0.04	-0.05	-0.03	-0.03	-0.04	-0.05	-0.02	-0.03	-0.04	-0.04
	V_{1b}	-0.02	-0.02	-0.03	-0.03	-0.02	-0.02	-0.02	-0.03	-0.01	-0.02	-0.02	-0.02
	B_1	0.07	0.08	0.08	0.09	0.06	0.07	0.08	0.09	0.06	0.06	0.07	0.08
	H_1	0.20	0.21	0.23	0.24	0.18	0.20	0.21	0.22	0.16	0.18	0.20	0.21
	N_{2a}	0.53	0.63	0.74	0.85	0.44	0.53	0.63	0.73	0.37	0.45	0.54	0.63
	N_{2b}	0.55	0.67	0.78	0.89	0.46	0.56	0.66	0.76	0.38	0.47	0.57	0.66
	T_{2a}	0.50	0.59	0.68	0.77	0.43	0.51	0.59	0.67	0.37	0.44	0.52	0.59
	T_{2b}	0.66	0.79	0.91	1.04	0.56	0.68	0.79	0.90	0.48	0.59	0.69	0.79
	V_{2a}	-0.15	-0.17	-0.18	-0.20	-0.14	-0.16	-0.18	-0.19	-0.13	-0.15	-0.17	-0.19
	V_{2b}	-0.10	-0.11	-0.12	-0.13	-0.10	-0.11	-0.12	-0.13	-0.09	-0.10	-0.11	-0.12
	B_2	0.39	0.39	0.40	0.41	0.39	0.40	0.41	0.42	0.40	0.40	0.41	0.42
	X	0.85	0.94	1.04	1.14	0.77	0.86	0.94	1.03	0.71	0.78	0.86	0.94
	Y	-0.15	-0.22	-0.29	-0.36	-0.09	-0.16	-0.22	-0.28	-0.05	-0.11	-0.16	-0.22

4. Structural dynamic characteristics analysis

4.1. Finite element model

In the finite element software Ansys, a numerical model with a span of 120 m was established. As an example, a set of parameters was chosen, which includes a span-to-rise ratio of 0.08, a thickness-to-span ratio of 0.10, and Case 1 of lower chord node arrangement scheme. The cable dome consists of two ring structures, with the inner ring structure having an opening diameter of 40 m. There are a total of 17 categories of components in the model. In the Ansys model, both cables and struts were simulated using the LINK180 element. Cables were defined as tension-only elements, while struts were defined as compression-only elements [20]. According to the initial prestress requirement, the cable cross-sections were prestressed to 20% of their breaking strength, while and the strut cross sections followed the aspect ratio design. For the cable, steel wire strands were used, and for the struts, hot-pressed seamless steel pipes were used. The material properties of these components can be found in Table 3. In the structural model, all nodes 3a in the outer ring were fully constrained as boundary conditions. The standard value for roof load is set to 0.5 kN/m^2, and it is applied by converting the distributed load into equivalent nodal loads using the SURF154 surface effect element for calculation. The structural model is depicted in Fig. 4. The initial prestress was applied through initial strains, and the levels of initial prestress and component cross-sectional parameters can be found in Table 4. The prestress mode was determined based on the values in Table 1. As shown in Table 4, the internal force distribution after the self-balancing of the finite element structural model matches the results of the prestressed state distribution, demonstrating the correctness of the established finite element model.

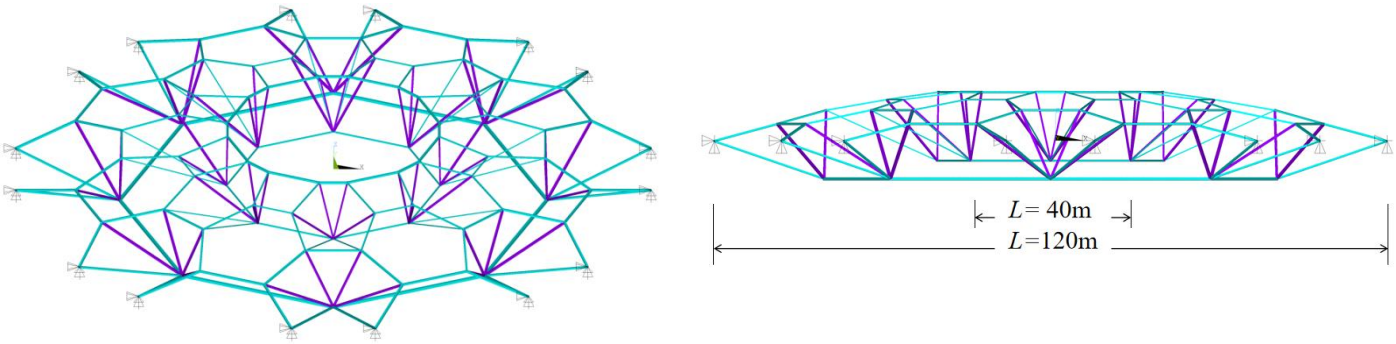

(a) 3D visualization of the numerical model (b) front view of the numerical model

Fig. 4 Numerical model of the $_{24}\bar{H}_{24\mathrm{III}}$ cable dome

Table 3
Material properties

Components	Yield strength (Mpa)	Poisson's ratio	Modulus of elasticity (Mpa)	Coefficient of linear expansion	Density (kg/mm^3)
cables	1860	0.3	1.95×10^5	1.36×10^{-5}	7.85×10^{-6}
struts	345	0.3	2.06×10^5	1.2×10^{-5}	7.85×10^{-6}

Table 4
Structural prestressing modes and member section parameters

Categorization	Components	Prestressed Mode	Self-equilibrating Internal Forces（kN）	Sectional Dimensions
Ridge cables	N_1	0.52	5235	Φ147
	N_{1a}	0.60	6030	Φ161
	N_{1b}	0.18	1760	Φ92
	N_{2a}	0.40	3962	Φ127
	N_{2b}	0.54	5448	Φ147
Diagonal cables	T_{1a}	0.23	2322	Φ80
	T_{1b}	0.27	2660	Φ107
	T_{2a}	0.49	4879	Φ147
	T_{2b}	0.60	5980	Φ155
Ring cables	B_1	0.11	1108	Φ92
	B_2	0.47	4699	Φ147
Sturts	H_1	0.22	2240	Φ80
	H_2	1.00	10000	Φ154
	V_{1a}	-0.03	-294	Φ254×14
	V_{1b}	-0.02	-231	Φ273×16
	V_{2a}	-0.11	-1082	Φ426×16
	V_{2b}	-0.08	-789	Φ427×15

4.2. Analysis of structural modal characteristics

The natural vibration characteristics are intrinsic mechanical properties of a structure that are closely related to its mass and stiffness. These characteristics not only reflect the stiffness of the structure but also directly influence the response to dynamic loads. They serve as an important basis for judging whether the distribution of structural stiffness and mass matches and is reasonable. Modal analysis includes two aspects: natural frequencies and mode shapes. The free vibration equation for each node are as follows:

$$[M]\{\ddot{u}\}+[C]\{\dot{u}\}+[K]\{u\}=0 \tag{10}$$

In the aforementioned equation, [M] represents the structural mass matrix, [C] represents the structural damping matrix, [K] represents the structural stiffness matrix, {F(t)} denotes the time-varying load function, $\{u\}$ is the nodal displacement vector, $\{\dot{u}\}$ is the nodal velocity vector, and $\{\ddot{u}\}$ is the nodal acceleration vector [15]. When conducting modal analysis, the influence of damping is not typically neglected. Therefore, the equation can be rewritten as follows:

$$[M]\{\ddot{u}\}+[K]\{u\}=0 \tag{11}$$

By performing a transformation on the equation, the generalized characteristic equation for the structure can be obtained as follows:

$$(K-\omega^2 M)\Phi=0 \tag{12}$$

In the equation, ω represents the structural natural frequencies, and Φ is the mode shape vector. The characteristic determinant of equation is given by:

$$\left|K-\omega^2 M\right|=0 \tag{13}$$

Solving the equation yields the n natural frequencies of the system denoted as $\omega_1 \le \omega_2 \le \ldots \le \omega_n$ and along with their corresponding mode shapes. In this study, the Block Lanczos method was employed for modal analysis, specifically considering the first 50 modes. The variation of natural frequencies is shown in Fig. 5. It is noteworthy that the first 10 natural frequencies of the structure exhibit proximity to each other, while the higher-order natural frequencies are more widely spaced. The fundamental frequency of the structure, measured at 1.0184 Hz, indicates that the structure has a relatively high stiffness. Due to the axial and central symmetry of the structure, the frequencies will appear in pairs with equal values.

From the data in Table 5, it can be observed that each pair of equal-frequency modes is essentially the same, except they are rotated 90° around the structure's central axis. As shown in Fig. 6, the modes for each order exhibit distinct characteristics. The 1st and 2nd modes are primarily dominated by vertical deformation in the inner ring, with horizontal displacement smaller than vertical displacement. The 3rd mode involves horizontal vibration, primarily characterized by circumferential deformation in the inner ring. In the 4th and 5th modes, vertical deformation dominates, with the point of maximum displacement shifting from the inner ring to the outer ring. Additionally, these modes exhibit significant horizontal displacement. The 6th and 7th modes are characterized by circumferential deformation in the outer ring, accompanied by vertical displacement. The 8th and 9th modes primarily exhibit vertical vibrations, with vertical deformation in the outer ring as the dominant feature. These modes also exhibit significant horizontal displacement. The 10th mode involves coupled deformation in both the circumferential and vertical directions, with slightly larger vertical displacement observed in the inner ring compared to horizontal displacement in the outer ring. Based on the analysis provided, it can be concluded that, for this cable dome configuration, the inner ring has lower stiffness compared to the outer ring, and the structural stiffness in the vertical direction is weaker than that in the circumferential direction.

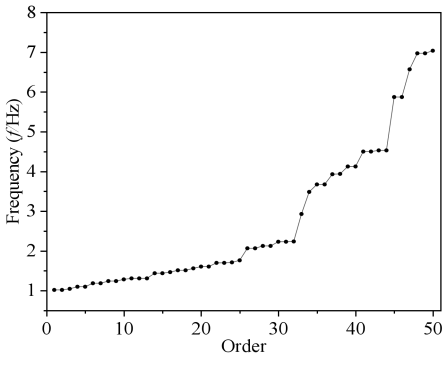

Fig. 5 The first 50 natural frequencies of the structure vs order numbers

Table 5
Material properties

Order	1、2	3	4、5	6、7	8、9	10
Frequency（Hz）	1.0184	1.0455	1.0991	1.1863	1.2417	1.2828

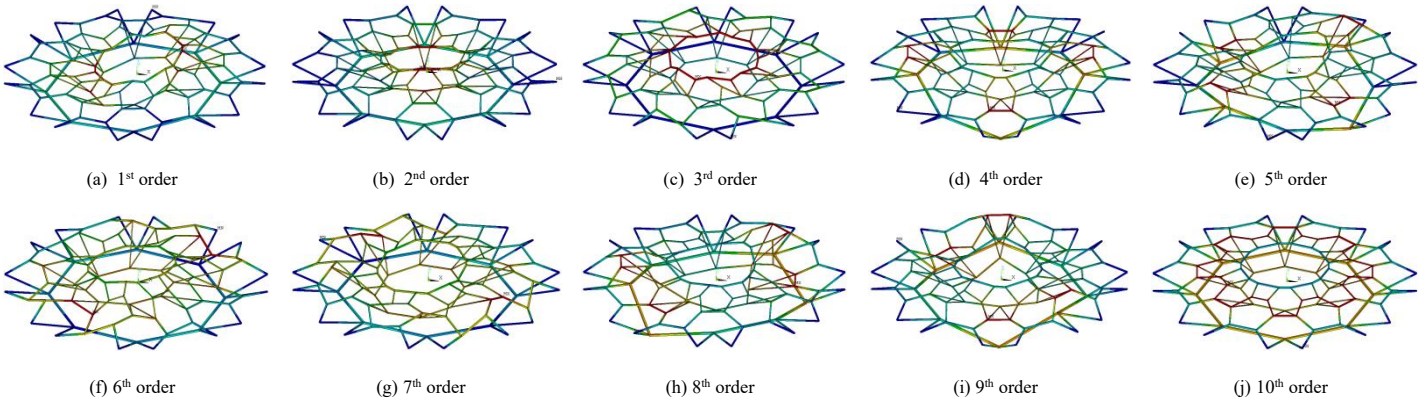

(a) 1st order (b) 2nd order (c) 3rd order (d) 4th order (e) 5th order

(f) 6th order (g) 7th order (h) 8th order (i) 9th order (j) 10th order

Fig. 6 The first 10 vibration modes of the structure

4.3. Parametric analysis of structural modal characteristics

The structural modal characteristics are closely related to factors such as the geometric configuration of the structure and the level of prestress. Therefore, it is essential to conduct a parametric analysis of the structural modal characteristics. To further investigate the influence of structural parameters on modal characteristics, several key structural parameters are selected, including the initial prestress level, span-to-rise ratio, thickness-to-span ratio and lower chord node arrangement scheme. Through parametric analysis, the impact of each parameter on the structural modal characteristics is explored.

4.3.1. Initial prestress level

To investigate the influence of the initial prestress level on the structural modal characteristics while keeping other parameters constant, the prestress levels are varied to be 0.5, 1.0, 1.5, and 2.0 times. Modal analysis is performed on the structure, and the resulting first 50 natural frequencies are shown in Fig. 6. From the figure, it is observed that, under different initial prestress levels, the trends in the first 50 natural frequencies of the structure remain generally consistent. The low-frequency modes are densely distributed, while the high-frequency modes are sparser and exhibit multiple jump points. As the initial prestress level increases, the natural frequencies of the structure also increase. The increase in low-frequency modes is more significant compared to the increase in high-frequency modes. Notably, when the prestress level changes from 0.5 times to 1.0 times, there is a significant increase in frequencies. However, as the prestress level changes from 1.0 times to 2.0 times, the rate of increase gradually decreases. This suggests that as the initial prestress level increases, the structural stiffness also increases. However, the rate of stiffness increase gradually decreases when the prestress level exceeds 1.0 times.

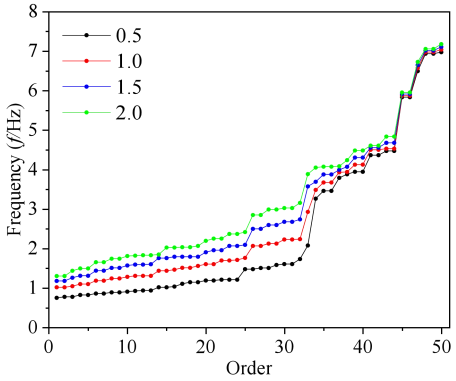

Fig. 6 The first 50 natural frequencies under different initial prestress level vs order numbers

4.3.2. Span-to-rise ratio

To explore the impact of the span-to-rise ratio on the structural natural frequencies while keeping other parameters constant, the structural model was analyzed with span-to-rise ratios of 0.07, 0.08, 0.09, and 0.10. The resulting first 50 natural frequencies of the structure are shown in Fig. 7 below. From the graph, it is observed that, for all four span-to-rise ratios, the overall trend of natural frequency variations is similar. The lower-order frequencies are denser, while the higher-order frequencies are sparser and exhibit multiple jump points. As the span-to-rise ratio increases, the natural frequencies decrease initially until around the 45th mode, after which they exhibit the opposite trend, increasing with a higher span-to-rise ratio. The span-to-rise ratio has a significant impact on the fundamental mode and lower-order frequencies, leading to changes in structural stiffness as the span-to-rise ratio increases.

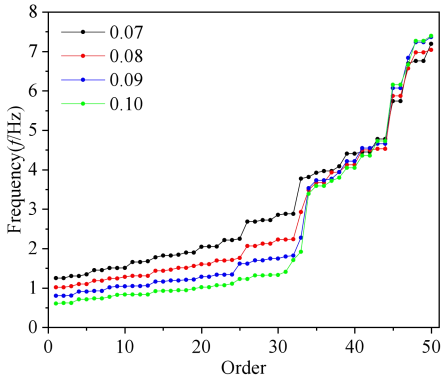

Fig. 7 The first 50 natural frequencies under different span-to-rise ratios vs order numbers

4.3.3. Thickness-to-span ratio

To investigate the impact of the thickness-to-span ratio on the structural natural frequencies while keeping other parameters constant, the structural model was analyzed with thickness-to-span ratios of 0.07, 0.08, 0.09 and 0.10. The resulting first 50 natural frequencies of the structure are shown in Fig. 8 below. From the figure, it is observed that, for all four thickness-to-span ratios, the overall trend of natural frequency variations is quite similar. The lower-order frequencies are denser, while the higher-order frequencies are sparser and exhibit multiple jump points. As the thickness-to-span ratio increases, the natural frequencies also increase. After the 45th mode, the natural frequencies of the three models with a thickness-to-span ratio greater than 0.08 become relatively close, indicating that the structural stiffness reaches its peak. An increase in the structural thickness-to-span ratio results in a corresponding increase in structural stiffness.

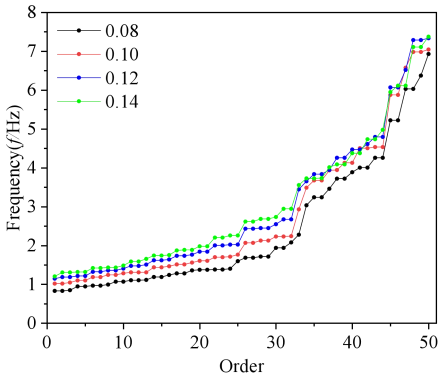

Fig. 8 The first 50 natural frequencies under different thickness-to-span ratios vs order numbers

4.4. Time history analysis of structural seismic

4.4.1. Selection and input of seismic waves

To understand the impact of seismic actions on this structure, this study

selected the El-Centro wave from the 1940 El Centro, California earthquake, which had a magnitude of 7.1, as the seismic load input. The numerical model employed in this section is the same as that in Section 4.1, with a damping ratio set to 0.02 [21]. The dynamic response of the structure under seismic loading was investigated. According to the guidelines outlined in the "Seismic Design Code for Buildings" Section 5.1.4, the analysis was conducted for high-intensity earthquake conditions in Seismic Design Category 8, with a maximum ground acceleration of 0.7 m/s² [22]. The El-Centro earthquake waveforms in three directions were adjusted to have peak accelerations of 0.7 m/s² in the X direction, 0.7 m/s² in the Y direction and -0.7 m/s² in the Z direction to meet the specific requirements. The acceleration time-history curves of the El-Centro earthquake waveforms for the first 30 seconds after adjustment are shown in Fig. 9.

The seismic response analysis of the structure was conducted using the dynamic time-history analysis method [14]. The structure's dynamic response was computed under one-dimensional, two-dimensional and three-dimensional seismic load inputs. The earthquake arrays used in the analysis are listed in Table 6. The seismic excitation factors were set to 1.0 and 0.65 for the two-dimensional seismic wave, and 1.0, 0.85, and 0.65 for the three-dimensional seismic wave.

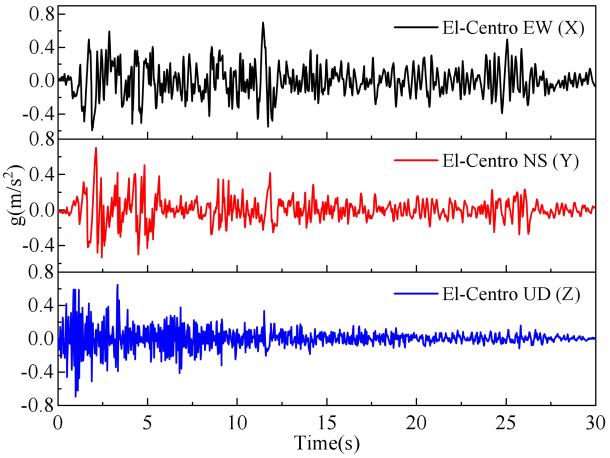

Fig. 9 The acceleration time-history curve for the first 30 s after amplitude adjustment of El-Centro seismic wave

Table 6
The excitation factors of each earthquake array

Arrays	X(EW)	Y(NS)	Z(U)
1D seismic wave	1.0	—	—
2D seismic wave	1.0	—	0.65
3D seismic wave	1.0	0.85	0.65

4.4.2. Internal force analysis

The calculation results of dynamic internal force coefficients for the structure under three different seismic arrays are shown in Table 7. Dynamic internal force coefficient refers to the ratio of the maximum internal force of a component during the time-varying internal force process to its initial internal force. Analyzing the data from Table 7, it can be concluded that the overall dynamic effect on component internal forces in the structure under seismic actions is not significant, with a maximum dynamic internal force coefficient of only 1.0031. In general, the internal forces of inner ring components exhibit a greater dynamic response to seismic actions compared to outer ring components. The dynamic response of internal forces induced by three-dimensional and two-dimensional seismic actions is significantly larger than that induced by one-dimensional seismic actions. Furthermore, the structural dynamic response to three-directional seismic actions is slightly greater than that to two-dimensional seismic actions.

Fig. 10 shows the time-history curves of the components that exhibit the most pronounced dynamic response under seismic actions among various types of components. During the analysis process, no tension cables exhibited any slackening phenomenon, and the distribution of dynamic responses coincided with the acceleration time-history curves of the seismic waves.

Table 7
The dynamic internal force coefficients of each component under different earthquake arrays

Components		Dynamic internal force coefficient of each component		
		1D	2D	3D
Ridge cables	N_1	1.00072	1.00260	1.00257
	N_{1a}	1.00285	1.00256	1.00256
	N_{1b}	1.00244	1.00291	1.00284
	N_{2a}	1.00230	1.00207	1.00207
	N_{2b}	1.00257	1.00229	1.00257
	T_{1a}	1.00235	1.00252	1.00254
	T_{1b}	1.00281	1.00277	1.00278
	T_{2a}	1.00243	1.00220	1.00237
	T_{2b}	1.00289	1.00263	1.00284
Diagonal cables	B_1	1.00215	1.00251	1.00295
	B_2	1.00217	1.00241	1.00259
Ring cables	H_1	1.00159	1.00191	1.00213
	H_2	1.00123	1.00187	1.00200
Struts	V_{1a}	1.00205	1.00218	1.00290
	V_{1b}	1.00297	1.00302	1.00310
	V_{2a}	1.00202	1.00214	1.00249
	V_{2b}	1.00217	1.00295	1.00227

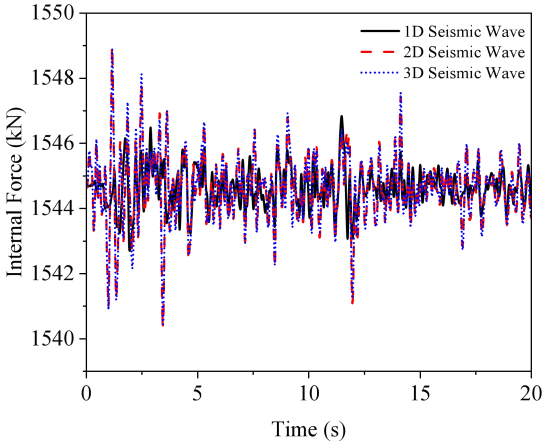

(a) The time-history curve of N_{1b}

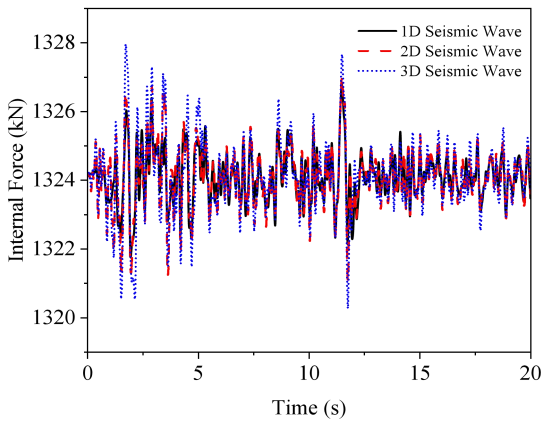

(b) The time-history curve of B_1

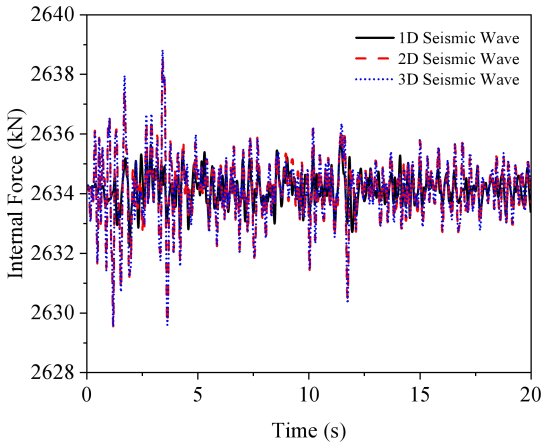

(c) The time-history curve of H_1

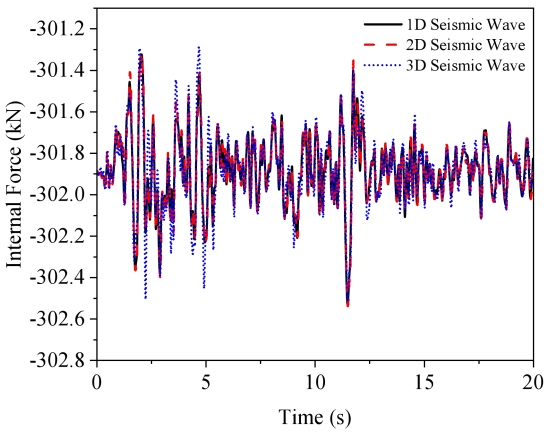

(d) The time-history curve of V_{1b}

Fig. 10 The time-history curve of internal forces in components under seismic loading

4.4.3. Deformation analysis

The seismic wave input direction and the substructure numbering for the cable dome structure are shown in Fig. 11. Along the X-axis, nodes are parallel to the one-dimensional horizontal seismic load direction, while along the Y-axis, nodes are perpendicular to the one-dimensional horizontal seismic load direction. Therefore, the maximum horizontal displacement in the X-direction occurs at nodes along the X-axis. Table 8 below presents the calculated dynamic displacement responses of various nodes in the cable dome structure under multi-dimensional seismic loads. Considering the horizontal symmetry of the structure in terms of height, the analysis of horizontal displacement primarily focuses on the X-direction.

Regarding the horizontal displacement of the structure, an analysis of the calculation results in Table 8 reveals that, due to the additional constant load acting only on the upper chord nodes, the X-direction horizontal displacement response at each upper chord node is greater under two- and three-dimensional seismic loads compared to one-dimensional seismic loads. Under two- and three- dimensional seismic loads, the dynamic responses are similar. For the lower chord nodes, under all three seismic arrays, the displacement dynamic responses are relatively close. The four braces converge at the lower chord node, providing sufficient lateral stiffness for the upper chord honeycomb cable grid. Therefore, the X-direction horizontal displacement dynamic response coefficients for all upper chord nodes are less than 1.10. The maximum displacement response coefficient is observed at inner ring lower chord node 1, with a coefficient of 1.54, which is significantly greater than the outer ring's coefficient of 1.03. This discrepancy is attributed to the lower pre-tension level of the inner ring cables, resulting in significantly lower radial stiffness for the inner ring. The time-history curves of horizontal displacement for the lower chord nodes are shown in Fig. 12.

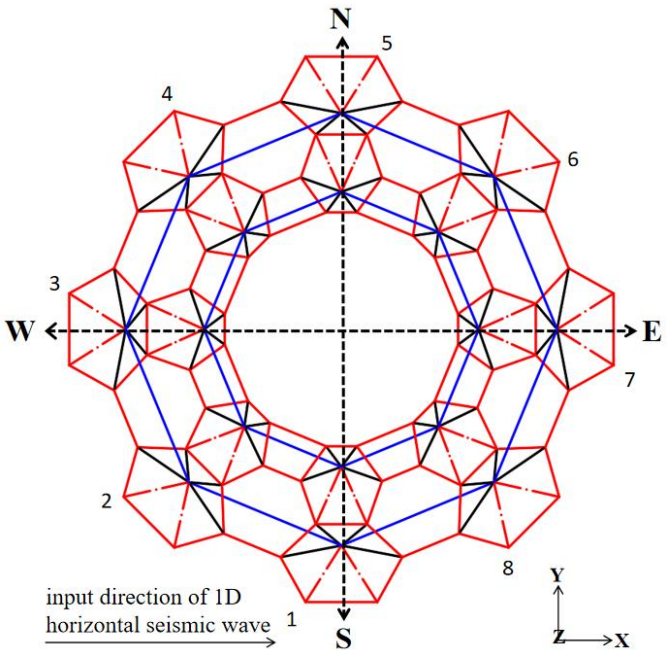

Fig. 11 Earthquake wave direction and substructure numbering

Table 8

The dynamic internal force coefficients of each component under different earthquake arrays

Node number		1_a			1_b			2_a			2_b			1’			2’		
Direction		1D	2D	3D	1D	2D	3D	1D	2D	3D	1D	2D	3D	1D	2D	3D	1D	2D	3D
U_x	U_{xmax}	6.50	6.53	6.52	7.82	7.86	8.00	7.53	7.57	7.56	7.17	7.20	7.21	4.83	4.85	4.86	12.55	12.57	12.58
	U_{x0}		6.06			7.45			7.01			6.96			3.15			12.27	
	U_{xmax}/U_{x0}	1.07	1.08	1.08	1.05	1.06	1.07	1.07	1.08	1.08	1.03	1.03	1.04	1.53	1.54	1.54	1.02	1.02	1.03
U_y	U_{ymax}	6.39	6.40	6.70	7.90	8.14	8.48	7.40	7.48	7.93	7.00	7.05	7.14	3.16	3.16	4.3	12.27	12.27	12.54
	U_{y0}		6.06			7.45			7.01			6.96			3.15			12.23	
	U_{ymax}/U_{y0}	1.05	1.06	1.11	1.06	1.09	1.14	1.06	1.07	1.13	1.01	1.01	1.03	1.00	1.00	1.37	1.00	1.00	1.03
U_z	U_{zmax}	91.90	92.10	92.37	81.65	81.77	82.94	57.03	57.18	57.56	39.61	39.64	40.15	91.05	91.63	92.12	56.32	56.36	56.71
	U_{z0}		-90.68			-81.19			-56.23			-39.23			-90.40			-55.43	
	U_{zmax}/U_{z0}	1.01	1.02	1.03	1.01	1.01	1.02	1.01	1.02	1.03	1.01	1.02	1.03	1.01	1.02	1.03	1.01	1.02	1.03

Note: U represents displacement, and subscripts with letters represent the direction of displacement. U_0 represents the initial load state displacement. The displacement dynamic response coefficient is the ratio of the maximum displacement in a certain direction to the initial load state displacement.

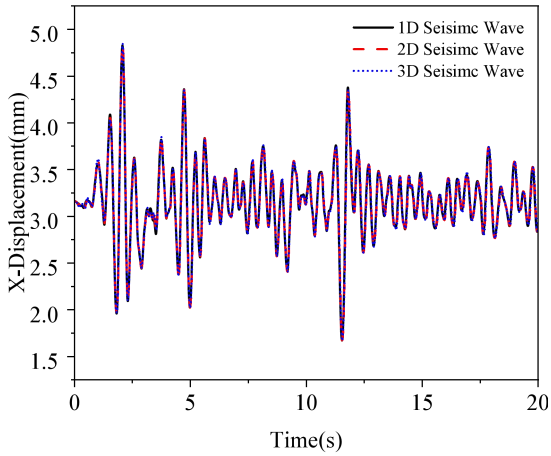

(a) The horizontal displacement time-history curve for lower chord node 1'-7

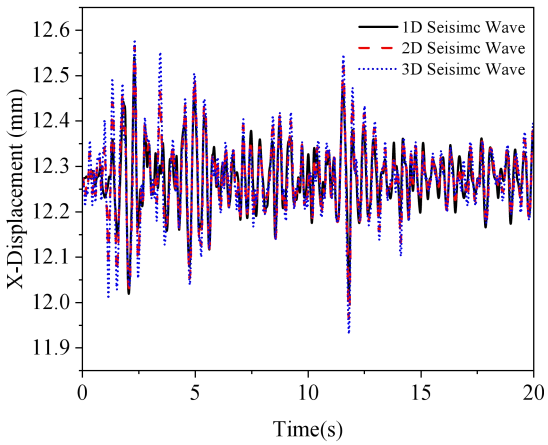

(b) The horizontal displacement time-history curve for lower chord node 2'-7

Fig. 12 The horizontal displacement time-history curve of lower chord nodes

Regarding the horizontal displacement of the structure, in seismic arrays 2 and 3, seismic waves were introduced in the Z-direction. Consequently, under two-dimensional and three-dimensional seismic loads, the vertical displacement dynamic response at various structural nodes is greater than that under one-dimensional loads. However, under one-dimensional and two-dimensional seismic loads, the dynamic response is similar. When comparing the results for upper chord nodes and lower chord nodes, it is evident that node loads have a relatively small impact on the Z-direction displacement of the nodes. When comparing the displacement values between inner and outer ring nodes, it can be observed that Z-direction seismic waves have a greater impact on the inner ring of the structure than the outer ring, indicating that the inner ring of the structure has lower stiffness than the outer ring. The time-history curves of vertical displacement for inner ring nodes are shown in Fig. 13, and the displacement fluctuations align with the acceleration time-history curves.

Overall, the dynamic response of the structure under seismic loads is relatively small. However, each type of components and nodes exhibits distinct dynamic responses to different seismic actions. The analysis results reflect the structural characteristics that are essential to consider when conducting dynamic load calculations and structural design for this cable dome structure. These findings are of significant importance.

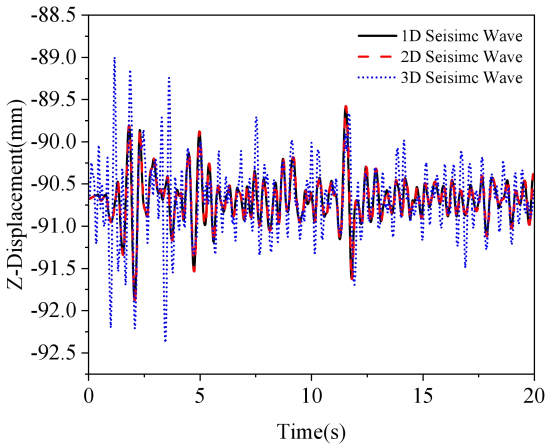

(a) The vertical displacement time-history curve for lower chord node 1_a-1

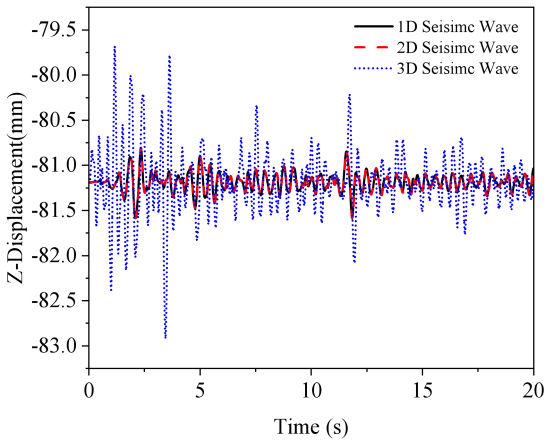

The vertical displacement time-history curve for lower chord node 1_b-1

Fig. 13 The vertical displacement time-history curve of inner ring nodes

5. Conclusions

This study focuses on the new form ${}_{24}\bar{H}_{24III}$ cable dome structure. Based on the node equilibrium theory, it derives general calculation formulas for the prestress state of the structure and the internal forces in the bars. Additionally, the study analyzes the distribution of prestress within the structure and how it changes with variations in structural parameters. Using a finite element numerical model with a span of 120 meters as an example, the study explores the impact of structural parameters on the structural vibration characteristics through modal analysis. Based on the modal analysis results, the study calculates the dynamic response of the components and critical nodes' displacements under multi-dimensional seismic loads using nonlinear dynamic analysis methods. These research findings provide valuable insights into the mechanical performance of the structure. The main conclusions of this paper are as follows:

(1) From the perspective of structural topology, the cable grid of the ${}_{24}\bar{H}_{24III}$ cable dome structure is uniformly distributed, making the structural design simple and efficient while minimizing the use of cables and struts. By tensioning the outer ring cables simultaneously, the structure can be pre-positioned, reducing the steps involved in tensioning during construction. This design approach can accommodate diverse architectural requirements while remaining cost-effective.

(2) The results of the prestressed state calculation example indicate that, the internal forces in the prestressed cables and struts of the structure are reasonably distributed, with the outer ring of the structure primarily governing the overall stiffness. Meanwhile, variations in the aspect ratio, height-to-span ratio and the arrangement of lower chord nodes have distinct effects on the distribution of internal forces in the cables and struts. Increasing the thickness-to-span ratio while moderately reducing the span-to-rise ratio can enhance the structural stiffness. However, this change would also lead to increased support reactions.

(3) The modal analysis results show that the fundamental frequency of the structure is 1.0184, indicating good stiffness. Due to the structural height symmetry, there is a distinct pattern in the resonant modes of the structure. These modes predominantly involve vertical deformations, suggesting that the vertical stiffness of the structure is comparatively weaker than the radial stiffness. Additionally, structural parameters have a noticeable impact on the resonant characteristics. Increasing the initial prestress level, reducing the span-to-rise ratio or increasing the thickness-to-span ratio can effectively enhance the structural stiffness.

(4) From the results of the seismic response calculations, the dynamic responses of various structural components and nodes do not significantly

differ from those under static loads. This indicates that the ${}_{24}\bar{H}_{24|||}$ cable dome structure, as a flexible system, demonstrates excellent seismic performance when reasonable structural parameters are selected under specific site conditions.

Acknowledgments

The work was financially supported by the National Natural Science Foundation of China (No. 52268031), which is gratefully acknowledged.

References

[1] Fuller, R.B. “Tensile-Integrity Structure”, U.S Patent, 3063521, 1962.
[2] Geiger, D.H., “The design and counstruction of two cable domes for Korean Olympics”, In Proceedings of the Membranes and Space Frames IASS Symposium, Osaka, Japan, 15–19, September, 1986.
[3] Geiger, D.H. “Roof structure”, U.S Patent, 4736553, 1998.
[4] Levy, M.P. “The Georgia dome and beyond achieving light weight-long span structure”, In Proceedings of the IASS-ASCE International Symposium, Atlanta, 560-562, 1994.
[5] Jian. Lu, S.D. Xue, X.Y. Li, et al., "Segmented Assembly Construction Forming Method Without Brackets of Spatial Cable-Truss Structure Without Inner Ring Cables", Advanced Steel Construction, 18(3), 687-698, 2022.
[6] X.F. Yuan, S.L. Dong, “New forms and initial prestress calculation of cable dome”, Engineering Mechanics, 22(2), 22-26, 2005.
[7] S.L. Dong, Z.H Wang, X.F. Yuan, “Static behavior analysis of a space structure combined of cable dome and single-layer lattice shell”, Journal of Building Structure, (03), 1-8, 2010.
[8] S.L. Dong, Y. Tu, “Configuration and prestress distribution of honeycomb-type cable dome with four struts”, Spatial Structures, (02), 3-12, 2018.
[9] S.L. Dong, Y. Tu, “Reserch on the system of honeycomb-type cable dome structures”, In Proceedings of the 18th National Symposium on Modern Structural Engineering, 7-12, 2018.
[10] S.L. Dong, H. Lv, Z.Q. Chen et al., “Structural form and initial prestress analysis on drum-shaped honeycomb-type cable with quad-strut layout”, Spatial Structures, 28(04), 3-15, 2022.
[11] Pellegrino S, Calladine C R. “Matrix analysis of statically and kinematically indeterminate frameworks”, International Journal of Solids and Structures, 22(4), 409-428, 1986.
[12] Pellegrino S, “Structural computation with the singular value decomposition of equilibrium matrix”, International Journal of Solids and Structures, 30(21), 3025-3035, 1993.
[13] X.F. Yuan, S.L. Dong, “The concept of integral feasible prestressing of cable dome structure and its application”, China Civil Engineering Journal, 34(2), 33-37, 2001.
[14] P.C. Li, “Nonlinear stability behaviour of cable-stiffened single-layer latticed shells under earthquakes”, International Journal of Structural Stability and Dynamics, 18(10), 1850117, 2018.
[15] Z.W. Lin, C. Zhang, J.C. Dong, et al., “Dynamic Response Analysis of Multiple Square Loops-String Dome under Seismic Excitation”, Symmetry, 13, 2062, 2021.
[16] H. Zhang, H. Lv, Z.Y. Zhu, et al., “Dynamic Response of the Component Failure of Drum-Shaped Honeycomb-Type III Cable Dome with Quad-Strut Layout”, Buildings, 13(8), 1894, 2023.
[17] C.Zhu, X.S Wu. “Reconstructing Dynamic Responses and Screening High-Precision Unmeasured Points for Geiger Cable Dome Structures”, Engineering Mechanics, 1-13, 2024.
[18] A.L Zhang, W. Wen, Y.X. Zhang, et al., “Static performance analysis of alternated cable dome with single and double brace struts”, Journal Of Vibration And Shock, 41(12), 321-330, 2022.
[19] X.F. Yuan, S.L. Dong, “The concept of integral feasible prestressing of cable dome structure and its application”, China Civil Engineering Journal, 34(2), 33-37, 2001.
[20] H.C. Liu, S.L. Dong, Y.D. Wang, “Structural morphological analysis and optimal design of a ribbed-type suspen-dome as stadium canopy with quad-strut layout and large central opening”, Journal of Building Structures, 44(9), 135-150, 2023.
[21] Z. Cao, S.D. Xue, X.S. Wang, “Selection of earthquake waves and values of damping ratio for space structures in aseismic analysis”, Spatial Structures, 14(3), 3-8, 2008.
[22] “Seismic Design Code for Buildings”, China Architecture Publishing & Media Co. Ltd, Beijing, 2010.